Applied Acoustics 220 (2024) 109963

Contents lists available at ScienceDirect

Applied Acoustics

journal homepage: www.elsevier.com/locate/apacoust

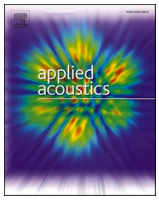

Wood chip sound absorbers: Measurements and models

Maedeh Lashgari [a], Ebrahim Taban [b], Mohammad Javad SheikhMozafari [c], Parham Soltani [d], Keith Attenborough [e,*], Ali Khavanin [a,*]

[a] Department of Occupational Health Engineering, Faculty of Medical Sciences, Tarbiat Modares University, Tehran, Iran
[b] Department of Occupational Health Engineering, School of Health, Mashhad University of Medical Sciences, Mashhad, Iran
[c] Department of Occupational Health Engineering, School of Public Health, Tehran University of Medical Sciences, Tehran, Iran
[d] Department of Textile Engineering, Isfahan University of Technology, Isfahan, Iran
[e] School of Engineering and Innovation, The Open University, Walton Hall, Milton Keynes MK7 6AA, United Kingdom

ARTICLE INFO

Keywords:
Wood chip
Johnson-Champoux-Allard
Johnson-Champoux-Allard-Lafarge
Slanted parallel identical uniform slits
Non-uniform pore size distribution
Finite element method
Sustainable panel absorber

ABSTRACT

Normal incidence absorption coefficient spectra of samples made from glued wood chips have been measured for various mesh sizes, bulk densities, thicknesses, and air gaps. Increasing thickness introduces additional layer resonance peaks and shifts the initial peak towards lower frequencies. The wood chip samples composed of the smallest mesh sizes were found to offer the highest sound absorption, comparable with that of the same thickness of materials made from synthetic fibers. Measured absorption spectra are compared with predictions of four models for the acoustical properties of rigid porous media. These include a model for slanted parallel identical uniform slits (SS), the Johnson-Champoux-Allard (JCA) and Johnson-Champoux-Allard-Lafarge (JCAL) models for arbitrary pore structures, and model for a non-uniform pore size distribution (NUPSD). Porosity and flow resistivity values have been determined non-acoustically. However, the tortuosity and characteristic lengths required for the JCA model have been obtained by fitting the measured absorption spectra. The thermal permeability required for the JCAL model has been deduced indirectly from the fitted tortuosity through a relationship with standard deviation of the pore size distribution due to the NUPSD model. JCAL and JCA models give the best agreement overall, but predictions of the SS and NUPSD models that use only the fitted tortuosity in addition to measured porosity and flow resistivity are found to give comparable agreement with data for many samples. SS and NUPSD predictions are improved by increasing the tortuosity values compared with those obtained by fitting the JCA model. The study should encourage the creation of sustainable sound-absorbing materials from wood chip wastes.

1. Introduction

Concern with noise pollution has increased with economic advancement, technological growth, and urban expansion. The adverse consequences of noise exposure include auditory effects, which range from auditory fatigue to severe cases of deafness, and non-auditory effects including heightened blood pressure, accelerated breathing rate, the onset of cardiovascular ailments, digestive disorders, behavioral and psychological anomalies, stress, and sleep disturbances [1]. The World Health Organization (WHO) has suggested that approximately 10 % of the global population faces the risk of developing noise-induced hearing loss (NIHL) due to exposure to hazardous sound pressure levels, with occupational noise accounting for 16 % of these cases [2]. One estimate is that 10 % of the European workforce is subjected to sound pressure levels considered highly hazardous [3]. Most of the materials employed for sound absorption consist of synthetic and inorganic fiber materials [4–7]. Despite their excellent sound absorption, their manufacture and deployment results in environmental pollution and adverse health effects on individuals, such as respiratory and skin problems. A critical limitation is the fact that they are not recyclable once their service life concludes. Incineration is not a viable option since it leads to the generation and release of harmful gases. Furthermore, their industrial production contributes to elevated emissions of carbon dioxide, methane, and nitrogen oxides due to high energy consumption [8]. An approach to improving indoor acoustics, while also addressing environmental concerns, is to use natural and sustainable materials to create sound absorbers. To this end, numerous countries have implemented legislation mandating the adoption of sustainable and biodegradable

* Corresponding authors.
E-mail addresses: keith.attenborough@open.ac.uk (K. Attenborough), khavanin@modares.ac.ir (A. Khavanin).

https://doi.org/10.1016/j.apacoust.2024.109963
Received 19 November 2023; Received in revised form 27 February 2024; Accepted 4 March 2024
Available online 10 March 2024

Table 1
A concise review of research on sound absorbers made from natural materials.

Material	Key findings	Year	Ref
Wood-based pulp fiber foams	Pulp fiber foams offer sound absorption characteristics that are on par with those of more conventional porous materials and are improved by additional processing and reducing fiber dimensions.	2021	[13]
Wood-based materials	Experiments on 17 different wood-based materials, commonly used in furniture design and manufacturing, show that, in the frequency range between 125 and 500 Hz, the wood surface layers with a lower density and higher porosity exhibit the highest sound absorption.	2015	[14]
Insulwood	1 cm thick Insulwood, with porosity 0.93, has a high noise-reduction coefficient (NRC) of 0.37 over the frequency range from 250 to 3,000 Hz.	2023	[15]
Luffa	The panels' sound absorption average (SAA) values ranged from 0.16 to 0.68, with thickness and density having a significant effect. The optimal characteristics for luffa panel fabrications were found to be 40 mm thickness, 225 kg/m^3 density, and 7.5 % binder content.	2024	[16]
Fruit stone	The study explored the sound absorption properties of panels made from different fruit stones. Smaller stones with higher surface roughness, especially in the crushed form, exhibit superior sound absorption, particularly at lower frequencies. Crushed samples outperform uncrushed ones, and introducing an air gap enhances absorption between 400 and 600 Hz.	2024	[17]
Kapok	Incorporating kapok fibers in conjunction with coir fibers notably enhanced the sound absorption coefficient of coir fibers. Additionally, it was observed that combinations of layers increased the frequency bandwidth of absorption.	2023	[18]
Corn husk	Corn husk samples exhibit impressive noise reduction coefficients, ranging from 0.36 to 0.60. Both the Dunn and Davern (DD) model and an adapted DD model utilizing the Nelder-Mead simplex algorithm were employed to predict the acoustic performance of the samples, the latter model demonstrated exceptional predictive accuracy.	2023	[19]
Coconut	NRC values exhibited a trend of growth with the thickness of the sound absorber. Specifically, NRC values were 0.20 for a 20 mm thickness, 0.32 for a 35 mm thickness, and 0.43 for a 50 mm thickness. Moreover, the peak sound absorption coefficient value was 0.83 at 3651 Hz for the 20 mm thickness. 0.76 at 2564 Hz for a 35 mm thickness, and 0.88 at 1435 Hz for the 50 mm thickness.	2023	[20]
Sugarcane bagasse	The prepared samples exhibited Sound Absorption Average (SAA) and Noise Reduction Coefficient (NRC) values within the range of 0.26 to 0.64 and 0.27 to 0.62, respectively, highlighting the commendable performance of SBW fibers, particularly at low- and mid-frequencies. Moreover, predictions using both the JCA model and statistical models were in good agreement with the data.	2022	[21]
Reed	The material under investigation demonstrates commendable acoustic and thermal qualities, with an absorption coefficient falling within the range of 0.6 to 0.9, at medium-frequencies.	2022	[22]
Wheat	The absorption coefficient of wheat fibers was deemed satisfactory at frequencies exceeding 3000 Hz. Elevating the pressure during sample fabrication led to an augmentation in the absorption coefficient so that wheat fibers represent a viable alternative to synthetic counterparts.	2021	[23]
Rice	The combination of rice husk and kenaf fibers yielded significantly superior results compared to the use of either kenaf fibers or rice husk in isolation. Predictions of the JCA model were in good agreement with data.	2021	[24]
Jute	Jute fiber samples with a thickness of 30 mm and a density of 1000 kg/m^3, exhibited the highest absorption coefficient at a frequency of 5000 Hz. The study confirmed the efficacy of jute fibers as both an industrial barrier and sound-absorbing material.	2021	[25]
Yucca Gloriosa (YG)	For specimens with thicknesses of 20 and 40 mm, the peak of sound absorption coefficient (SAC) occurs at frequencies of 3150 Hz and 2000 Hz, respectively. This investigation confirmed that YG fibrous samples efficiently absorb and dissipate acoustic energy.	2020	[26]
Esparto grass	Increasing material thickness and introducing an air cavity between the material and the rigid backing surface resulted in observable increases in low-frequency sound absorption. However, the empirical Delany and Bazley model tended to underestimate sound absorption at lower frequencies, a known limitation of this semi-empirical model.	2020	[8]
Sisal	At a frequency of 1600 Hz, the absorption coefficient of sisal fiber samples approached unity. The Delaney-Bazley model was less successful in predicting the sound absorption coefficient than the JCA model.	2019	[27]
Coir	The absorption coefficient increased with frequency. By augmenting the material's thickness under constant density conditions increased the absorption coefficient, particularly at frequencies below 1000 Hz. The JCA model demonstrated superior accuracy in predicting sound absorption in comparison to the Delany–Bazley and Miki models.	2019	[28]
Flax	Between 250 and 4000 Hz, flax fiber samples demonstrated a superior absorption coefficient to glass fiber sample of the same thickness. Notably, the sound absorption coefficient of flax fibers exceeded 0.5 above 1000 Hz.	2018	[29]
Kenaf	For sample densities between 140 and 150 kg/m^3 and thicknesses between 25 and 30 mm, the absorption coefficient was approximately 0.5 at 500 Hz, and 0.85 at frequencies exceeding 1500 Hz. Furthermore, it was observed that augmenting both density and thickness led to an expansion of the absorption bandwidth.	2018	[30]
Kenaf	Adding kenaf fibers to PU foam significantly improved acoustic absorption across all frequencies. The optimized sample had an SAA of 0.65.	2023	[31]
Banana	The measured absorption coefficients of banana fiber samples between 500 and 6000 Hz were 0.11 for untreated fibers and 0.12 for fibers treated with epoxy. The study further inferred that banana fibers represent a viable substitute for synthetic fibers.	2017	[32]
Different natural fibers	An inverse method was used for predicting the acoustical properties of nine natural fibers, including six vegetative fibers (kenaf, wood, hemp, coconut, straw, and cane), one animal fiber (sheep wool), recycled	2017	[33]

(*continued on next page*)

Table 1 (*continued*)

Material	Key findings	Year	Ref
	cardboard, and granular cork. The study reveals that using such natural sources leads to favorable sound absorption characteristics.		

materials. This regulatory effort aims to endorse environmentally friendly materials, curtail polluting procedures, and foster the production of recyclable goods [9]. There is an increasing interest, particularly within the automotive and construction sectors, in the fabrication and advancement of acoustic panels constructed from natural materials as a sustainable alternative to synthetic fiber materials like rock wool, glass wool, and glass fibers [10,11].

After reviewing the range of sustainable materials that have been proposed for sound absorption, the manufacture of the wood chip samples is described in Section 2 along with measurements of their physical properties. Also, Section 2 reports measurements of porosity and flow resistivity, and describes four models used to predict the normal incidence absorption coefficient of the wood chip samples. The effects of sample thickness, density and wood chip mesh size and comparisons between measurements and models are discussed in Section 3. Concluding remarks are in Section 4.

1.1. Acoustical performance of natural materials

The growing emphasis on natural and recycled materials in recent years is driven not only by their contribution to reducing environmental and health impacts but also by their cost-effectiveness. These factors have gained considerable attention in the quest for more sustainable and economically viable solutions. Related research falls into two broad categories: the first encompasses studies solely dedicated to the utilization and examination of raw natural fiber materials, while the second category involves investigations that use natural fibers as reinforcement within a polymer matrix, commonly referred to as Bio-composites [8]. Natural fibers may be categorized into five primary types: (1) bast fibers, exemplified by jute, flax, cannabis, ramie, and kenaf; (2) leaf fibers, including banana, sisal, agave, and pineapple; (3) seed fibers, such as coir, cotton, and kapok; (4) grass and reeds, represented by wheat, maize, and rice; and (5) miscellaneous types encompassing roots and wood. Some plants, for instance, jute, flax, hemp, and kenaf produce both bast and core fibers, while agave, coconut, and palm oil contain both fruit and stem fibers. Furthermore, cereal grains exhibit the presence of both stem and hull fibers [12].

Table 1 presents a summary of studies on the use of natural materials as sound absorbers.

Table 1 confirms that many naturally based materials offer useful sound absorption and provide viable sustainable alternatives to sound absorbers made from synthetic and inorganic fibrous materials.

Recycling and reusing wood waste has the potential to reduce environmental pollution and provide cost-effective raw materials for various applications. In Iran, the annual consumption of wood is approximately 5 million cubic meters, with over 1 million cubic meters being imported. However, the recycling rate for cellulose materials in Iran is only around 2 %, while European countries have achieved a recycling rate exceeding 70 %. This indicates a significant disparity in the utilization of wood waste as a valuable resource in Iran compared to European countries. Wood, as a natural composite, possesses notable characteristics such as high porosity, low density, strong strength, and excellent resistance to UV radiation. These properties have led to numerous investigations exploring the use of wood waste for sound absorption purposes. However, so far, no measurements and predictions of the acoustic properties of materials composed of beech fibers and Indian wood chips and shards have been reported.

This paper describes the manufacture of wood chip samples with different thicknesses and composed from each of five different particle sizes together with non-acoustical measurements of porosity, flow resistivity, and measurements of their normal incidence sound absorption coefficients in an impedance tube without and with air gaps. Also, the performances of four models for predicting the measured absorption coefficient spectra are investigated. The microstructures assumed by the models include those slanted parallel identical uniform slits (SS), arbitrary pore structures (models of Johnson-Champoux-Allard (JCA) and Johnson-Champoux-Allard-Lafarge (JCAL)), and non-uniform pores characterized by a log-normal size distribution (NUPSD). The characteristic dimensions and tortuosity required by the JCA model in addition to measured porosity and flow resistivity, were obtained by fitting absorption coefficient data using the differential evolution algorithm and the finite element method (FEM) using COMSOL® and MATLAB software.

Table 2
Mesh sizes and resulting wood chip particle sizes.

Mesh NO	Average particle length (mm)	Average particle width (mm)
4	4.97 ± 2.05	2.15 ± 1.45
8	4.85 ± 2.07	1.57 ± 0.73
10	3.14 ± 1.13	1.51 ± 0.56
12	2.65 ± 1.37	1.11 ± 0.32
16	1.27 ± 0.63	0.61 ± 0.31

Table 3
Sample thickness, binder, particle constituent weights, and density.

Sample No	Mesh NO	Thickness (mm)	Binder (g)	Wood (g)	Density before Adding Binder (g/cm^3)	Density after Adding Binder (g/cm^3)
1	4	20	55.2	27.6	0.176	0.196
2	4	30	74	37	0.157	0.176
3	4	40	102	50.85	0.162	0.183
4	4	50	120	59	0.150	0.177
5	8	20	45.37	30.25	0.193	0.211
6	8	30	64	42.56	0.181	0.202
7	8	40	81	54	0.172	0.201
8	8	50	103.81	69.21	0.176	0.201
9	10	20	48.37	32.25	0.205	0.236
10	10	30	64	43.53	0.150	0.231
11	10	40	84	56.3	0.179	0.223
12	10	50	137.5	76.42	0.195	0.212
13	12	20	55.2	34.85	0.222	0.250
14	12	30	64	43.7	0.186	0.235
15	12	40	90	59.68	0.190	0.206
16	12	50	117.61	78.40	0.200	0.218
17	16	20	55.50	37	0.236	0.264
18	16	30	75.39	50.26	0.213	0.242
19	16	40	81.58	64.39	0.205	0.222
20	16	50	100.02	75.25	0.192	0.224

2. Materials and methodology

2.1. Preparation of samples

Samples have been fabricated by gluing beech and Indian wood chips and fragments from the furniture manufacturing industry. The wood chips were passed through meshes to sort them into five distinct size classes. Table 2 list the mesh sizes and the corresponding average lengths and widths of the wood chips. The glue was polyvinyl alcohol (PVA), which is a colorless or cream-colored granule that is odorless, environmentally friendly, and water-soluble. It is an ideal binding agent for natural fibers because of its non-toxicity, high degradability, high polarity, and resistance to oil, solvent, and grease. PVA glue with a 7.5 % concentration was made by dissolving 7.5 g of PVA granules in 100 ml of distilled water. Subsequently, the solution was stirred at 80 °C and 500

Fig. 1. Wood chips Sample preparation and acoustic absorption testing.

Table 4
Non-acoustically measured and acoustically fitted parameters of the samples.

Sample	Thickness d (mm)	Average Bulk density ρ (kg/m^3)	Bulk density ρ (kg/m^3)	Flow resistivity σ ($Nm^{-4}s$)	Porosity ϕ (%)	Tortuosity α_∞	Characteristic lengths	
							$\Lambda(\mu m)$	$\Lambda'(\mu m)$
1	20	165	176(±11)	5880(±160)	72.5	2.2	240	380
2	30		157(±8)	5590(±105)	72.5	2.4	200	500
3	40		162(±3(	5310(±210)	72.5	1.8	230	410
4	50		150(±15)	4980(±230)	72.5	1.3	290	550
5	20	182	193(±11)	6010(±140)	69.6	3	190	300
6	30		181(±1)	5710(±190)	69.6	2.61	202	260
7	40		172(±10)	5460(±150)	69.6	2.35	138	370
8	50		176(±6)	5140(±215)	69.6	2.4	190	350
9	20	190	205(±15)	6160(±130)	68.4	1.23	58	140
10	30		183(±7)	5860(±115)	68.4	2.08	97	360
11	40		179(±11)	5580(±160)	68.4	2.1	160	291
12	50		195(±5)	5240(±190)	68.4	2.2	180	290
13	20	203	222(±19)	6260(±205)	66.1	1.5	73	120
14	30		186(±19)	5940(±160)	66.1	1.9	66	150
15	40		190(±13)	5690(±155)	66.1	2.1	130	160
16	50		199(±4)	5350(±130)	66.1	2.2	115	165
17	20	220	236(±16)	6390(±180)	63.3	2.2	70	130
18	30		213(±7)	6080(±145)	63.3	2.2	66	194
19	40		205(±15)	5760(±160)	63.3	1.9	65	226
20	50		204(±16)	5410(±150)	63.3	1.96	75	350

rpm using a magnetic stirrer for 150 min. To prepare cylindrical samples with diameters of 30 and 100 mm, corresponding to the internal diameters of the impedance tubes, polyethylene molds were designed of varying thicknesses and filled with wood chips. The desired amount of wood chips was determined by filling the mold to the desired thickness. Afterward, the wood chips were weighed using a digital scale model SMA-FR262. A preliminary investigation was conducted to determine the amount of glue needed to attain the desired consistency of the samples without filling the gaps between wood chip particles. The wood chips were sorted into various mesh sizes, and it was found that a glue content of 1.5 times the weight of wood chips was suitable for samples with mesh sizes 8, 10, 12, and 16, while a weight of 2 times that of wood chips was required for samples with mesh 4 because of the large particle size. Table 3 lists the properties of the samples.

After thoroughly mixing wood chips and PVA, the resulting blend was deposited into a polyethylene mold. Mechanical pressure was applied to the mold for 8 h. Subsequently, the samples underwent a 12-hour drying process employing a hot air blower. The completely dry samples were then weighed and their dry weight was used to calculate bulk density. Fig. 1 shows the sequence of steps involved in the sample fabrication process.

2.2. Measurements

2.2.1. Thickness and bulk density

The thickness and areal density of cylindrical specimens were measured according to guidelines outlined in ASTM D1037, "Standard Test Methods for Evaluating Properties of Wood-Based Fiber and Particle Panel Materials". To determine their thickness, three measurements were taken for each sample at different locations using a digital thickness gauge. A precision digital balance manufactured by Shimadzu Corporation with model number BX300 was used for the thickness measurement. Each sample was measured 10 times to ensure accuracy and consistency in the results. The bulk density of the specimens was obtained by dividing their mass per unit area by their corresponding thickness. Equation (1) was used to determine porosity, Φ:

$$\Phi = 1 - \frac{\rho_b}{\rho_w} \tag{1}$$

where ρ_b denotes the bulk density, while ρ_w signifies the density of

wood, which is 490 kg/m^3 for wooden chips. The results are given in Table 4

2.2.2. Flow resistivity

Flow resistivity (σ) was measured in accordance with ISO 9053 "Acoustics: Determination of Airflow Resistance, Part 1: Static Airflow Method." The flow resistivity was calculated from.

$$\sigma = A\frac{(p_2 - p_1)}{Qd} \tag{2}$$

where the variables p_1 and p_2 referred to the pressure at the front and back facets of the specimen, correspondingly. The variables A and d represent the cross-sectional area of the specimen and specimen thickness, respectively, while Q is the volumetric fluid flow through the specimen. In this method, a digital differential pressure gauge Testo 512 (Testo Co. Lenzkirch, Germany) was employed to measure the pressure drop at a given flow rate. A total of four tests were conducted for each specimen, and the average value was computed.

2.2.3. Sound absorption coefficient spectra

The normal incidence sound absorption coefficient (SAC) was measured in an impedance tube in accordance with ISO 10534-2 "Acoustics - Determination of sound absorption coefficient and impedance in impedance tubes Part 2: Transfer-function method". The impedance tube (Fig. 3) consisted of two microphones, a loudspeaker, and a frequency analysis system. Broadband random sound waves were generated by the loudspeaker and emitted at one end of the tube. These sound waves propagated towards the surface of the sample, which was securely placed in a sample holder located at the opposite end of the tube. The reflected signals at the two fixed microphones on the tube wall were analysed by the frequency analyser to determine the normal incidence absorption coefficient. Data processing was performed using the BSWA VA-Lab4 Basic software. Prior to the measurement procedure, the microphones were calibrated at a sound pressure level of 114 dB and a frequency of 1 kHz using the BSWA calibrator. The sound absorption coefficients were evaluated in the low-frequency range (63–1600 Hz) using a large diameter tube (100 mm) and in the high-frequency range (1600–6300 Hz) using a small diameter tube (30 mm). The sound absorption coefficient spectra reported in this study include measurements obtained from both tubes. For the measurements, samples of various thicknesses and bulk densities were inserted into the holders of the tubes. The position of the sample or the cavity behind it was manipulated using a rigid plunger. To ensure the reliability of the data, at least three separate measurements of the sound absorption coefficient were made on each sample. To minimize errors resulting from misalignment, the sample was repositioned before each sampling process. All experiments were conducted under controlled atmospheric conditions, including a temperature of (20 ± 2) °C, a relative humidity of (45 ± 10) %, and a pressure of 1.01325 × 105 Pa. The SAC spectra were measured on samples of four thicknesses (20, 30, 40, and 50 mm), containing particles with five distinct mesh sizes (4, 8, 10, 12, and 16), and with two air gap depths (10 and 30 mm) behind the samples.

3. Sound absorption coefficient predictions

Although direct measurement of the sound absorption coefficient is preferable in establishing the sound absorbing performance of porous materials; regrettably, the cost associated with an impedance tube setup, and the inconsistent availability of such equipment, coupled with the necessity for specialized acoustic laboratory facilities, may make direct measurements unfeasible. So it is of interest to investigate the extent to which the measured absorption coefficient spectra of wood chip samples with known flow resistivity and porosity can be predicted. Wood chip samples may be modeled as porous materials with a rigid frame, the acoustical properties of which are those of an equivalent effective fluid with a complex density, containing the influence of viscous effects, and a complex compressibility, containing the influence of thermal effects. The abilities of four models to predict the acoustical performance of wood chip samples have been compared. The models assume different microstructures and require different numbers of parameters. The model microstructures investigated are a) slanted parallel identical uniform slits (SS), arbitrary pore structures by means of the b) Johnson-Champoux-Allard (JCA), and c) Johnson-Champoux-Allard-Lafarge (JCAL) models and d) non-uniform pores with a log-normal distribution of sizes (NUPSD).

Each of these models is described in sections 2.1 to 2.3.

3.1. Identical uniform parallel slanted slits model (SS)

According to Stinson et al. [34], the complex density and complex compressibility in a (single) uniform pore of arbitrary shape, are written as:

$$\rho(\omega) = \rho_0/H(\lambda) \tag{3}$$

$$C(\omega) = (\gamma P_0)^{-1}\left[\gamma - (\gamma - 1)H\left(\lambda\sqrt{N_{Pr}}\right)\right] \tag{4}$$

where time dependence $e^{-i\omega t}$ is understood, ω is the angular frequency, the function $H(\lambda)$ has known analytical expressions for several ideal pore shapes, λ is a dimensionless parameter, $(\gamma P_0)^{-1} = \left(\rho_0 {c_0}^2\right)^{-1}$ is the adiabatic compressibility of air, γ, P_0 and N_{pr} denote the specific heat ratio of the pore fluid, atmospheric pressure, and Prandtl number respectively.

For a parallel-sided slit:

$$H(\lambda) = 1 - \tanh\left[\lambda\sqrt{(-i)}\right]/\lambda\sqrt{(-i)} \tag{5}$$

If the slit width is 2b, the dimensionless parameter $\lambda = b\sqrt{\omega/\nu}$, where $\nu = \mu/\rho_0$, μ being the dynamic coefficient of viscosity and ρ_0 the density of air. The viscous boundary layer thickness for laminar flow oscillations near a flat plate, $\delta = \sqrt{2\nu/\omega}$, so $\sqrt{2}/\lambda = \delta/b$ represents the frequency-dependent fraction of the slit pore semi-width occupied by the viscous boundary layer. A critical frequency (or 'roll over' frequency) [35] above which inertial forces dominate over viscous forces is given by $f_c = 3\nu/\left(2\pi b^2\right)$. At this critical frequency, $\sqrt{2/3}$ or 81.6 % of a slit is occupied by the viscous boundary layer. The thermal boundary thickness is $\delta/\sqrt{N_{PR}}$. Typically, this is much smaller than the viscous boundary layer.

The dimensionless parameter λ can be related to the (steady) flow resistivity (σ) of the bulk material by using the Kozeny-Carman formula [36]:

$$\sigma = \frac{2\mu\alpha_\infty s_0}{\phi {r_h}^2} \tag{6}$$

where, for a parallel-sided slit of semi-width b, the hydraulic radius $r_h = \frac{\text{"wetted" area}}{\text{perimeter}} = b$, and the steady flow shape factor $s_0 = 1$.

Consequently, the flow resistivity of a medium with uniform parallel slits is given by

$$\sigma = \frac{3\mu\alpha_\infty}{\phi b^2} \tag{7}$$

where ϕ represents porosity and α_∞ represents tortuosity.

Tortuosity accounts for the changes in direction and in cross-section which cause fluid flow in the pores to deviate from straight lines. It is defined as the square of the increase in path length per unit thickness of material due to deviations of the steady-flow path from a straight line. If the slits are uniform, parallel, and inclined at an angle θ to the surface normal:

$$\alpha_\infty = 1/(\cos\theta)^2 \tag{8}$$

The complex density ($\rho(\omega)$) and complex compressibility ($C(\omega)$) for the bulk material are calculated from those for an individual slit using Eqs. (9) and (10):

$$\rho_b(\omega) = (\alpha_\infty/\phi)\rho(\omega) \tag{9}$$

$$C_b(\omega) = \phi C(\omega) \tag{10}$$

The bulk propagation constant ($k(\omega)$) and relative characteristic impedance ($Z_C(\omega)$) of the porous material consisting of parallel slits of width $2b$ and edge-to-edge separation $b(1-\phi)/\phi$ are calculated from Eq. (11) and (12):

$$k(\omega) = \omega\sqrt{\rho_b(\omega)\, C_b(\omega)} \tag{11}$$

$$Z_C(\omega) = (\rho_0 c_0)^{-1}\sqrt{\rho_b(\omega)/C_b(\omega)} \tag{12}$$

The surface impedance of a hard-backed porous layer of thickness d is:

$$Z(d) = Z_C(\omega)\coth(-ik(\omega)d) \tag{13}$$

The plane wave reflection coefficient, $R(d)$, and normal incidence absorption coefficient, $\alpha(d)$, for a hard-backed porous layer are given by Eq. (14), and 15, respectively:

$$R(d) = \frac{\rho_0 c_0 - Z(d)}{\rho_0 c_0 + Z(d)} \tag{14}$$

$$\alpha(d) = 1 - \left|(R(d))^2\right| \tag{15}$$

In addition to layer thickness (d), the slanted identical parallel uniform slit model for the absorption coefficient of a hard-backed porous layer requires knowledge of three parameters: flow resistivity (σ), porosity (ϕ) and tortuosity (α_∞). The slit slant angle (θ) is determined from tortuosity through Eq. (8). The slit pore semi-width (b) is determined from tortuosity, flow resistivity, and porosity using Eq. (7).

3.2. Johnson-Champoux-Allard model (JCA)

To allow simultaneously for arbitrary pore shapes and for pore cross-sections that change along their lengths, viscous and thermal characteristic lengths have been introduced [37–39]:

The bulk complex density and compressibility functions are written as:

$$\rho_b(\omega) = \alpha_\infty\rho_0\left[1+\frac{i\sigma\phi}{\omega\rho_0\alpha_\infty}G(\Lambda)\right] \tag{16}$$

$$C_b(\omega) = (\gamma P_0)^{-1}\left[\gamma-(\gamma-1)\left[1+\frac{i\sigma\phi}{\omega\rho_0\alpha_\infty N_{Pr}}G'(\Lambda')\right]^{-1}\right] \tag{17}$$

where $G(\Lambda) = \sqrt{\left(1+\frac{4i\alpha_\infty{}^2\eta\omega\rho_0}{(\sigma_\rho\Lambda\phi)^2}\right)}$, $G'(\Lambda') = \sqrt{\left(1+\frac{4i\alpha_\infty{}^2\eta N_{Pr}\omega\rho_0}{(\sigma_C\Lambda'\phi)^2}\right)}$, Λ, Λ' are the viscous and thermal characteristic lengths respectively, $\sigma_\rho = \frac{8\mu\alpha_\infty}{\phi\Lambda^2}$ and $\sigma_C = \frac{8\mu\alpha_\infty}{\phi\Lambda'^2}$.

As well as porosity and flow resistivity, the JCA model requires values for tortuosity and the two characteristic lengths. It is difficult to obtain these values through non-acoustical measurements. Instead, in this study, values of these parameters for the wood chip samples have been obtained by fitting measurements of absorption coefficient spectra using a differential evolution algorithm described elsewhere and a finite element model of the impedance tube and sample arrangement [40].

3.3. Johnson-Champoux-Allard-Lafarge model (JCAL)

To improve the extent to which the JCA model accounts for the diffusion and trapping of air molecules at pore walls, the JCAL model [41] introduces the additional parameter of thermal permeability, k_0', or the related thermal flow resistivity $\sigma' = \mu/k_0'$.

In the JCAL model, Eq. (17) is replaced by,

$$C_b(\omega) = (\gamma P_0)^{-1}\left\{\gamma-(\gamma-1)\left[1+\frac{i\mu\Omega}{\omega\rho_0 k_0' N_{PR}\sqrt{1+\frac{\omega\rho_0 4k_0'^2 N_{PR}}{i\mu\Lambda'^2\Omega^2}}}\right]^{-1}\right\} \tag{18}$$

3.4. Non-uniform cylindrical pores with a log-normal radius distribution (NUPSD)

A model for non-uniform cylindrical pores with a log-normal radius distribution [42] introduces a Padé approximation for bulk complex density,

$$\rho_b(\omega) = (\alpha_\infty/\phi)\left[1+F_\rho(\varepsilon_\rho)/\left(\varepsilon_\rho{}^2\right)\right] \tag{19}$$

$$F_\rho(\varepsilon) = \frac{1+a_{\rho1}\varepsilon_\rho + a_{\rho2}\varepsilon_\rho{}^2}{1+b_{\rho1}\varepsilon_\rho} \tag{20}$$

where $\varepsilon_\rho = \sqrt{\left(\frac{-i\omega\rho_0\alpha_\infty}{\phi\sigma}\right)}$, $a_{\rho1} = \theta_{\rho1}/\theta_{\rho2}$, $a_{\rho2} = \theta_{\rho1}$, $b_{\rho1} = a_{\rho1}$, $\theta_1 = \frac{1}{3}$, $\theta_{\rho2} = e^{-\frac{1}{2}(\beta\log 2)^2}$, and β is the standard deviation of the pore size distribution in φ units such that a pore dimension in mm $= 2^{-\varphi}$.

The corresponding Padé approximation for bulk compressibility is:

$$C_b(\omega) = (\gamma P_0)^{-1}\left[\gamma-(\gamma-1)/\left(1+F_C(\varepsilon_C)/\left(\varepsilon_C{}^2\right)\right)\right] \tag{21}$$

$$F_C(\varepsilon) = \frac{1+a_{C1}\varepsilon_C + a_{C2}\varepsilon_C{}^2}{1+b_{C1}\varepsilon_C} \tag{22}$$

where $\varepsilon_C = \sqrt{\left(\frac{-i\omega\rho_0\alpha_\infty N_{Pr}}{\phi\sigma'}\right)}$, $a_{C1} = \theta_{C1}/\theta_{C2}$, $a_{C2} = \theta_{C1}$, $b_{C1} = a_{C1}$, $\theta_{C1} = \frac{1}{3}$, and $\theta_{C2} = e^{-\frac{3}{2}(\beta\log 2)^2}/\sqrt{2}$.

If the mean pore radius is $\bar{r}$, then:

$$\sigma = \left[\frac{8\mu}{\phi\bar{r}^2}\right]e^{6(\beta\log 2)^2} \tag{23}$$

$$\sigma' = \mu/k_0' = \left[\frac{8\mu}{\phi\bar{r}^2}\right]e^{-6(\beta\log 2)^2} \tag{24}$$

Also,

$$\alpha_\infty = e^{4(\beta\log 2)^2} \tag{25}$$

Eqs. (23)–(25) can be used to deduce that $\sigma' = \sigma e^{-12(\beta\log 2)^2}$ and that $\varepsilon_C = \varepsilon_\rho e^{6\beta\log 2}$.

If non-acoustical measurements of flow resistivity, porosity, and standard deviation (β) of the pore size distribution are available, the log-normal non-uniform pore model does not require either adjustable or fitted parameters. If a value for α_∞ is available after fitting data using the JCA model, as is the case for the wood chip samples, then β is determined through Eq. (25).

NUPSD [43] yields relationships between the characteristic lengths, mean pore dimension and standard deviation of the log-normal size distribution:

$$\Lambda = \bar{r}e^{-5/2(\beta\log 2)^2} \tag{26}$$

$$\Lambda' = \bar{r}e^{3/2(\beta\log 2)^2} \tag{27}$$

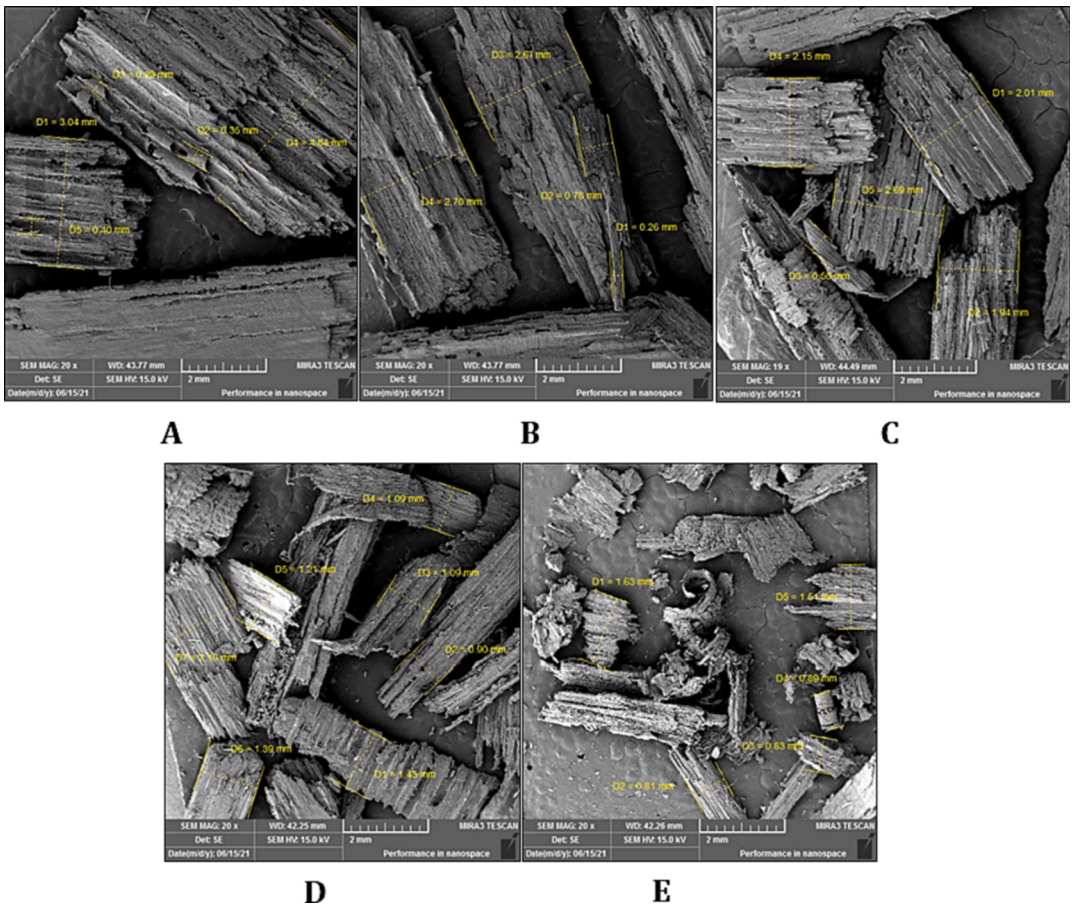

Fig. 2. FE-SEM image of wood chips in the mesh (A: 4, B: 8, C: 10, D: 12, and E: 16).

This means that the ratio of characteristic lengths, $\frac{\Lambda'}{\Lambda} = e^{4(\beta \log 2)^2}$, depends only on the standard deviation of the pore size distribution.

For the JCAL predictions reported in Section 2.3, the thermal permeability has been calculated using Eq. (24), and the value of β deduced from Eq. (25) with the fitted value of α_∞.

3.5. Finite element method (FEM) and COMSOL simulation

The Finite Element Method (FEM) and a model for the acoustical properties of rigid porous media, (JCA) has been used to simulate sound absorption in an impedance tube within the COMSOL® framework. The acoustic pressure within a predefined domain is determined by solving the Helmholtz equation:

$$Q = \nabla\left(\frac{-(\Delta p - q)}{\rho_0}\right) - \frac{\omega^2}{\rho_0 {c_s}^2} \tag{28}$$

where p denotes sound pressure ($\frac{N}{m^2}$), ρ_0 is air density ($\frac{Kg}{m^3}$), Q is an optional bipolar source ($\frac{N}{m^3}$), q represents an optional unipolar source ($\frac{I}{s^2}$), ω denotes the angular frequency ($\omega = 2\pi f$) and c_s is the speed of sound ($\frac{m}{s}$) and $\rho_0 {c_s}^2$ the volume modulus in terms of $\frac{N}{m^2}$.

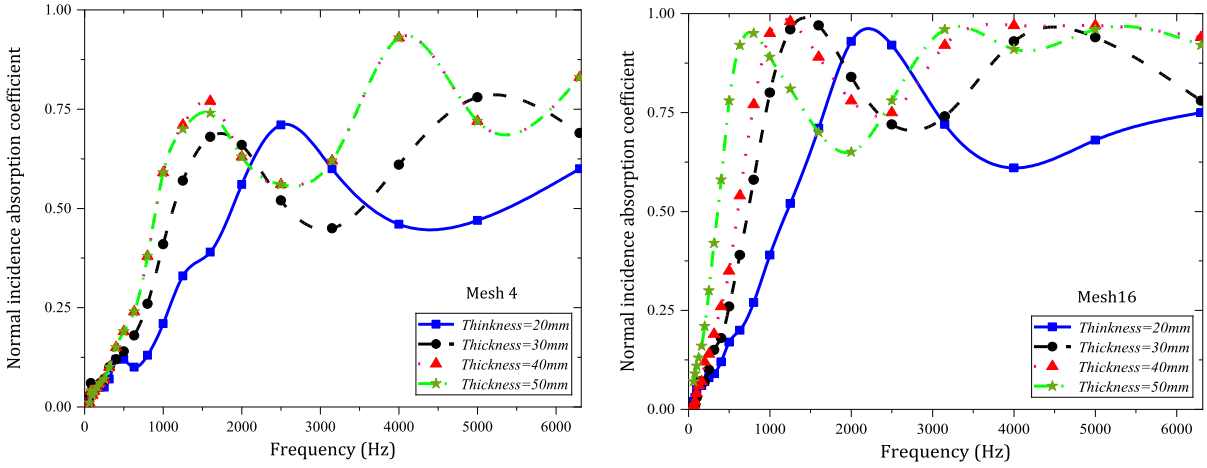

Fig. 3. Variation in measured absorption coefficient spectra with thickness and mesh size.

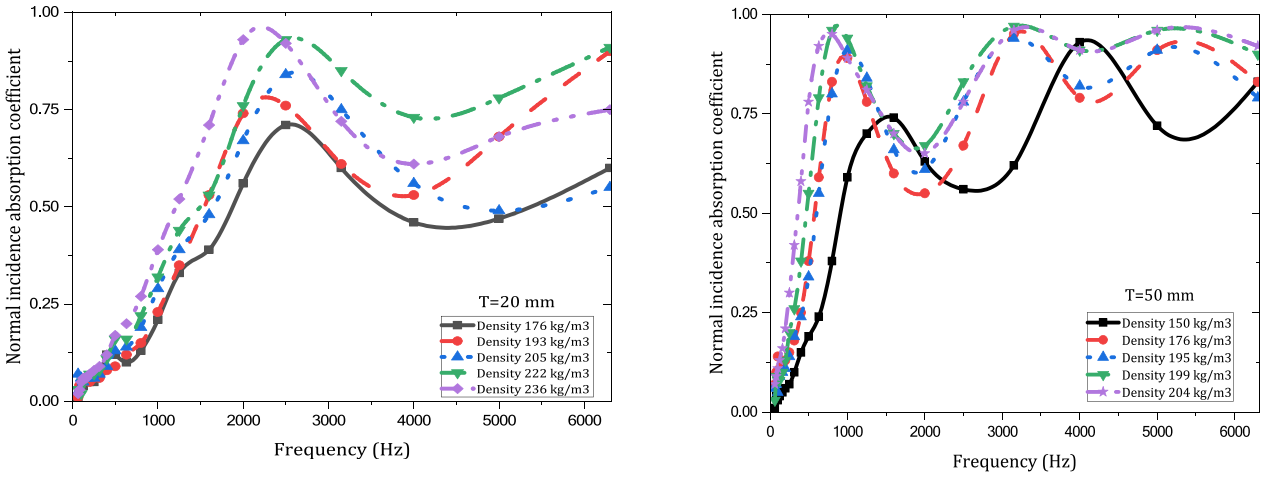

Fig. 4. The effect of bulk density on SAC.

In accordance with ISO10534-2, the FEM simulation assumes a rectangular configuration measuring 10 cm in length and 20 cm in width to represent the impedance tube. The FEM model employed in this study is composed of three distinct components: a perfectly matched layer (PML), a background pressure field (BPF), and the poroacoustics domain (PD).

The perfectly matched layer (PML) mitigates unwanted reflections within this domain. The background pressure field (BPF) delineates the trajectory of planar sound waves along the $z-$axis, tracing their path from the source to the sound absorber. Within the poroacoustics domain (PA), the attenuation and propagation behaviors of sound waves within porous materials are obtained by utilizing the framework of equivalent fluid theory (EFT). The JCA model was used to fit the data. To ensure precision in the results, the model's maximum mesh size was set at one-sixth of the minimum wavelength. This approach ensures finer resolution, enabling the capture of intricate acoustic phenomena within the porous structure. To simulate the impedance tube setup, calculations were made in the frequency range from 63 to 6300 Hz using FEM modeling and defining the geometry of the problem as a two-dimensional open rectangle with triangular meshing and a mesh size set at 1/6th of the shortest wavelength [44].

4. Results and discussions

4.1. Wood chip sample properties

Fig. 2 shows FE-SEM images of the wood chips at 20x magnification. Image processing techniques were used to obtain the particle width and lengths listed in Table 2.

Since the chips consist of aggregations of wood fibers, their surfaces are rough. Surface roughness contributes to sound absorption since it not only increases internal friction but also increases the internal surface area of the material thereby enhancing thermal exchange at pore walls.

4.2. Sound absorption parameters

Table 4 lists the measured and fitted parameters of the samples. As mentioned earlier, the porosity and airflow resistivity were measured directly. The additional three parameters (tortuosity, viscous characteristic length, and thermal characteristic length) required for the JCA model were determined through an inverse method employing the differential evolution algorithm and FEM. Finally, these parameters were entered as input data into COMSOL®.

The next three sub-sections report the influence of sample thickness, bulk density, and air gap backing on the acoustic characteristics of the wood chip samples.

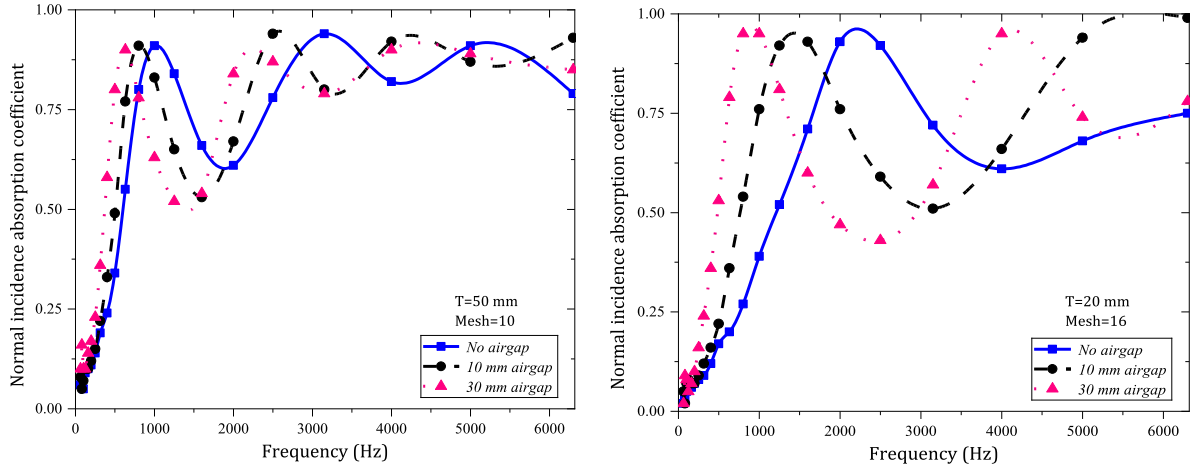

Fig. 5. The effect of the air gap behind the samples on SAC.

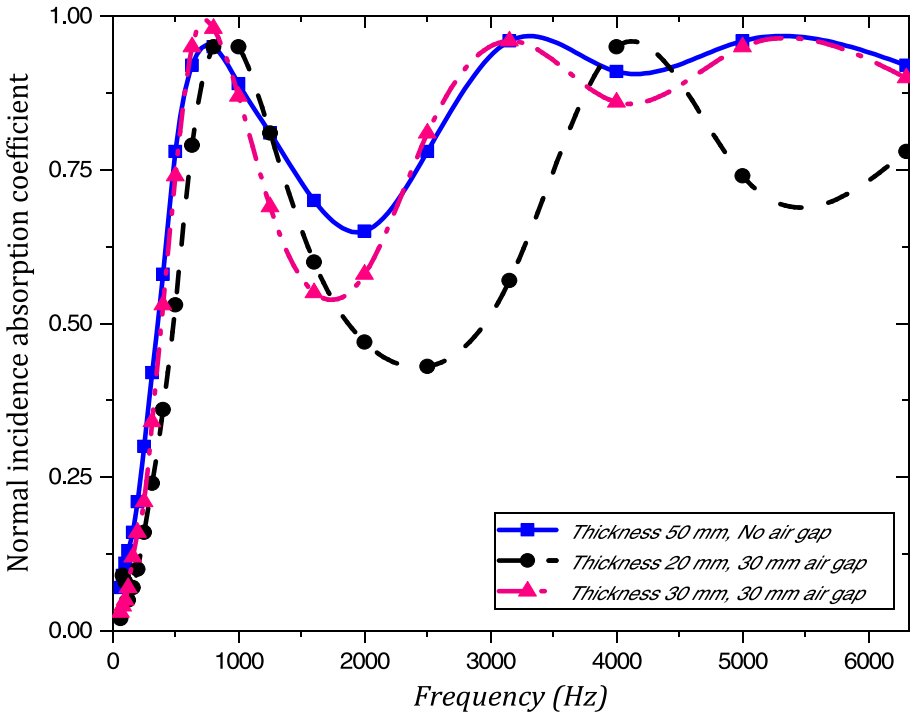

Fig. 6. Comparison of absorption coefficients in three sample configurations with and without air gap.

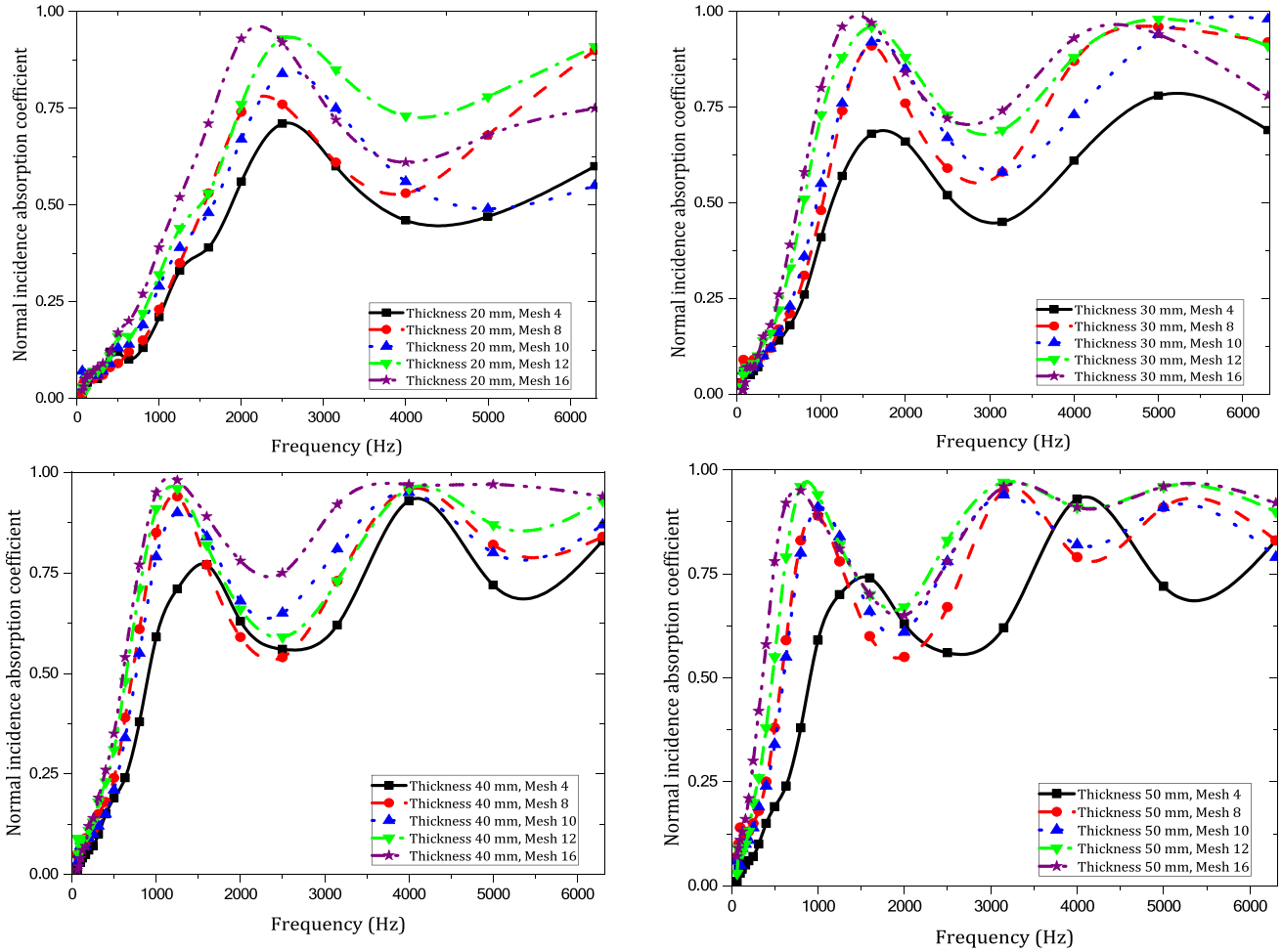

Fig. 7. The effect of wood chip mesh size on SAC of samples with the same thickness.

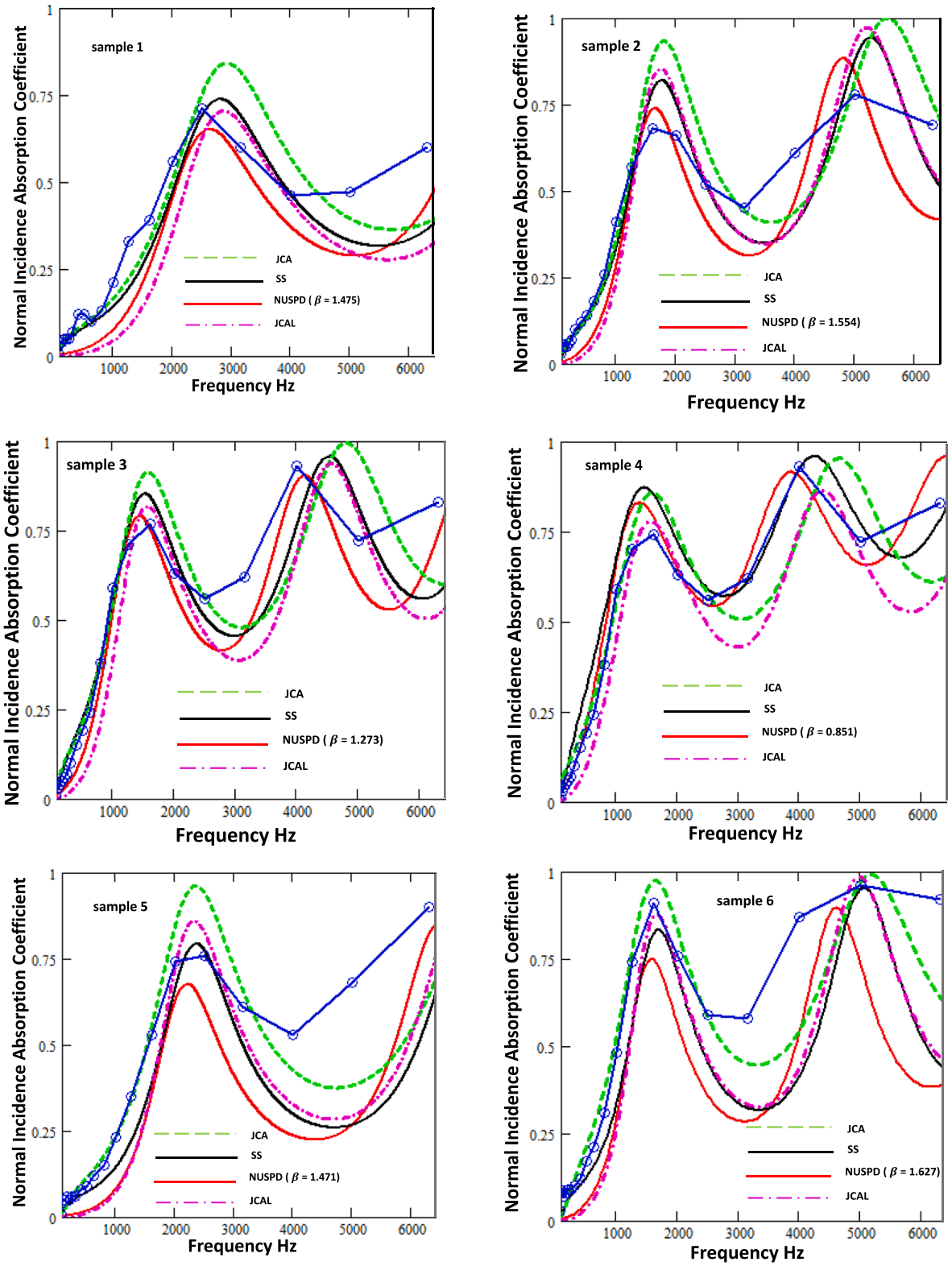

Fig. 8. Measured absorption coefficient spectra for twenty wood chip samples compared with predictions of four models.

4.2.1. The effect of thickness on SAC

Fig. 3 shows the effect of sample thickness on the acoustic behavior of wood chip samples with the largest and smallest mesh sizes.

As has been shown elsewhere for different materials [45,46], the absorption coefficient of wood chip samples increases with increasing frequency and sample thickness. The relatively low flow resistivity of the wood chip samples results in a strong quarter wavelength resonance i.e., when the thickness of the layer corresponds to a quarter wavelength (and an odd multiple thereof) of the sound wave inside the layer. Increasing thickness introduces additional resonance peaks while

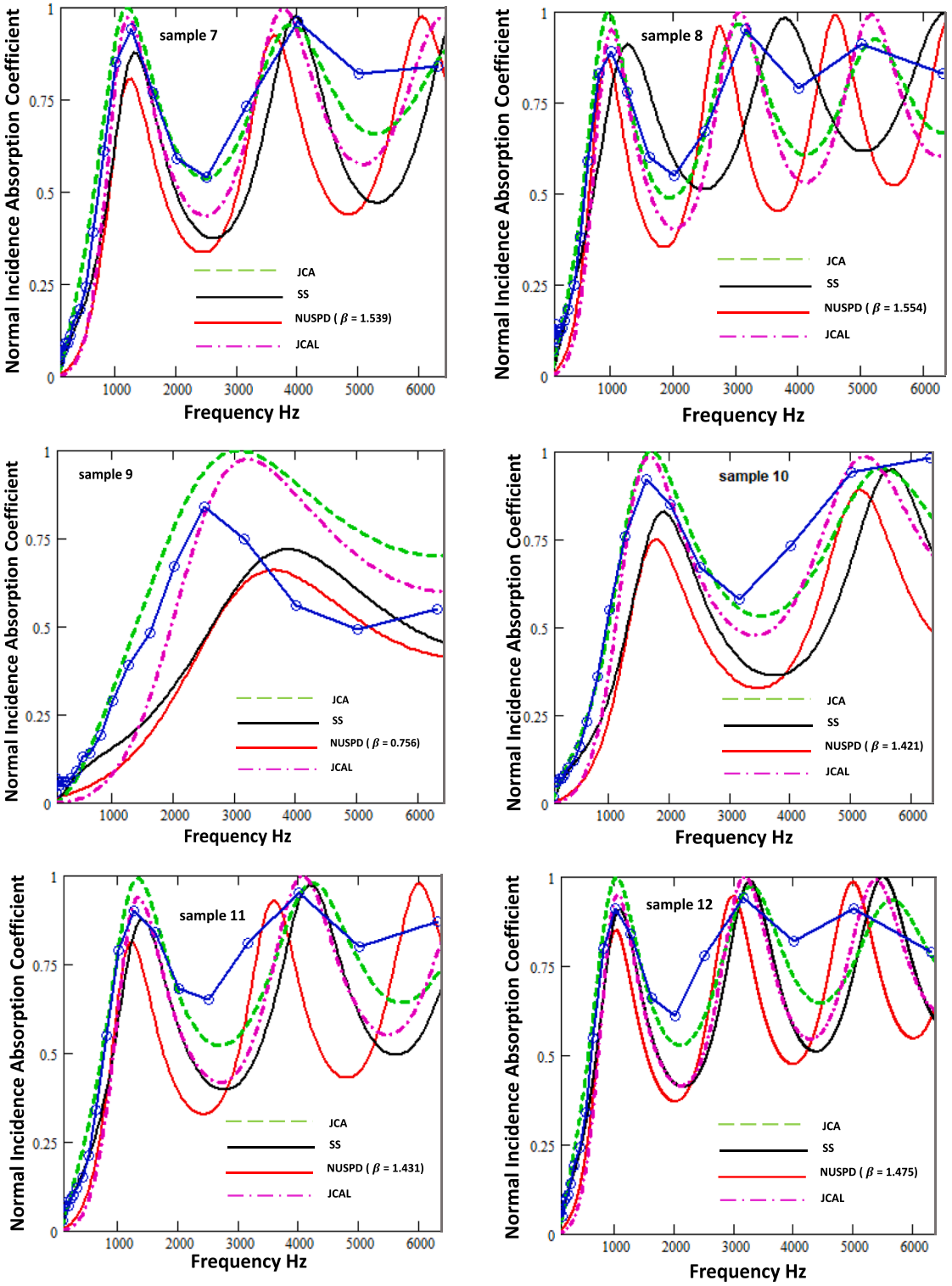

Fig. 8. (*continued*).

shifting the initial peak towards lower frequencies. The resonant nature of the absorption spectra is a disadvantage for broadband absorption compared with less resonant absorption characteristics such as achieved with the same thickness of synthetic fiber materials having much higher flow resistivity.

Nevertheless, with thicknesses of 30 mm, 40 mm, and 50 mm, the smaller mesh size and higher-density wood chip samples exhibit near-perfect absorption at 1000 Hz which would be useful for speech-related applications in building spaces.

4.2.2. *The effect of bulk density on SAC*

Fig. 4 shows the effect of bulk density on the sound absorption coefficient for the smallest and largest sample thickness. Increasing bulk density, at a given thickness, improves the absorption coefficient at lower frequencies.

However, beyond a certain density, the associated reduction in

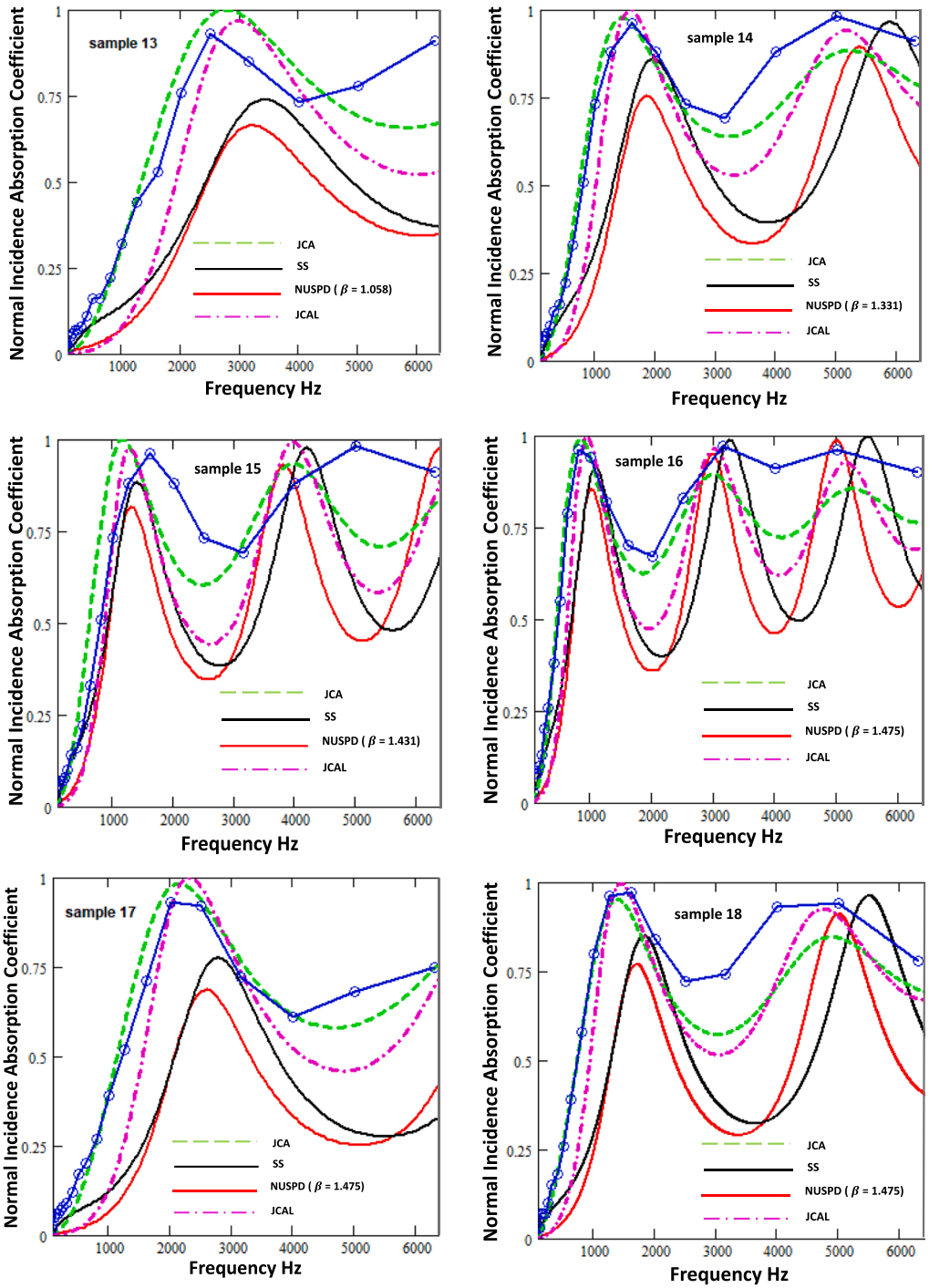

Fig. 8. (*continued*).

porosity reduces sound absorption. These results are consistent with previous research showing that an increase in density only leads to an increase in the absorption coefficient up to a point beyond which further increases can result in a subsequent reduction in absorption [21,47].

4.2.3. The effect of the air gap behind the samples on SAC

Typically, the absorption coefficients provided by porous materials are low at low frequencies. As well as increasing thickness and density, low-frequency absorption is increased by the introduction of an air gap behind the material. This reduces the need for additional material to increase thickness, thereby lowering production costs. Also, it results in reduced production time. Fig. 5 illustrates the outcomes of employing air gaps of 10 mm and 30 mm behind two thicknesses of wood chip materials composed of 50 mm (mesh 10) and 20 mm (mesh 16) particles.

Fig. 6 compares the absorption coefficient spectra for three configurations: a 50 mm sample without an air gap, a 20 mm sample with a 30 mm air gap, and a 30 mm sample with a 30 mm air gap behind it. As illustrated in Fig. 6, a 20 mm thick sample with a 30 mm air gap yields equivalent results to a hard backed 50 mm thick sample at frequencies below 1500 Hz. Furthermore, the absorption coefficient spectrum of a 30 mm material with a 30 mm air gap closely approximates that of a 50 mm material. Consequently, it can be asserted that, for the purpose of cost reduction and expediting sample production, air layers can be employed instead of increasing material volume and thickness, yielding

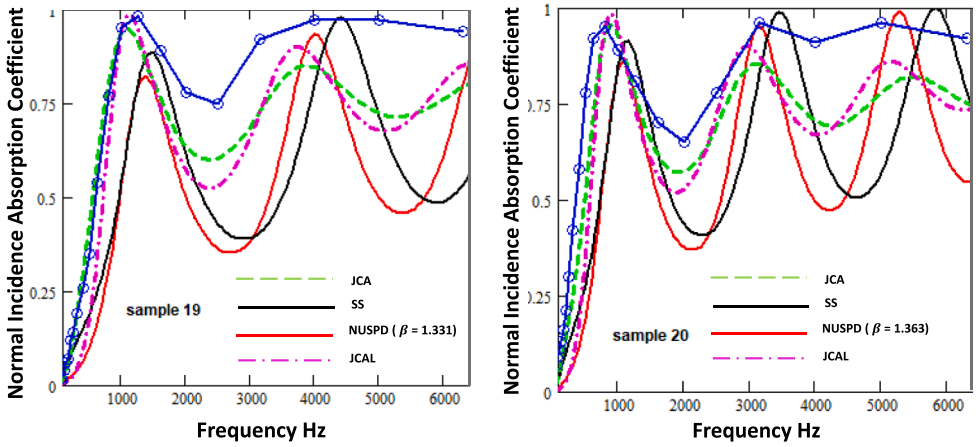

Fig. 8. (*continued*).

nearly identical outcomes. This may be important for indoor applications. A similar result is mentioned elsewhere [40].

4.2.4. *The effect of wood chip mesh size*

A significant drawback of natural materials compared with synthetic and inorganic counterparts like polypropylene, rock wool, and glass wool is their relatively low absorption coefficient. This discrepancy is primarily attributed to the larger diameter of grains obtained from natural sources and hence their lower flow resistivities than those of their synthetic counterparts [48]. The flow resistivity is increased by using smaller particles. In this study, five mesh sizes (4, 8, 10, 12, and 16) were employed. The influences of particle size on sound absorption spectra, while maintaining constant sample thickness, are shown in Fig. 7.

Fig. 7 illustrates that, for a given sample thickness, an increase in mesh size, which corresponds to a reduction in particle size, increases the absorption coefficient. This is a consequence of the increased flow resistivity (Table 4). However, the absorption peak moves towards lower frequencies. Normally this would imply an increase in tortuosity and hence the effective thickness [49].

4.3. *Comparison of models with data*

Fig. 8 compares predictions of the rigid porous medium models described in sections 2.1 to 2.3 with the absorption coefficient spectra measured on the wood chip samples having the dimensions and properties detailed in Tables 3 and 4. Tables 4 and 5 list the parameter values used in the calculations.

Consistently, the JCA and JCAL model predictions are in good agreement with data. To an extent, this is to be expected since the predictions use parameter values obtained by fitting the JCA model predictions to the data. The inclusion of the additional thermal permeability parameter required by the JCAL model using Eq. (15) with values of β deduced from fitted tortuosity values through Eq. (25) leads to minor improvements in the agreement with data compared with that obtained with the JCA model mainly at higher frequencies.

Nevertheless, the predicted absorption spectra show greater layer resonances than the data above 1 kHz. In part this is because the data are for one third octave frequency bands whereas the predictions are for 50 Hz wide bandwidths. If 50 Hz interval values were to be averaged over third octaves the predicted resonance magnitudes would appear to be less. Also, the resonances may be damped by attenuation mechanisms not included in the models. As mentioned in section 3.1, the wood chip surfaces are rough, which can increase sound absorption [17,49].

Despite requiring only values of tortuosity in addition to the measured flow resistivity and porosity, the SS and NUPSD models give predictions that are in useful agreement with data for most of the samples. Although the SS and NUPSD predictions for 20 mm thick samples 9, 13, and 17 give relatively poor agreement with data, it should be noted that the predictions have been made using tortuosity values obtained by fitting data with the JCA model which involves non unique fitting of three parameters. Moreover, as remarked earlier, the tortuosity values resulting from fitting with the JCA model are not consistent with the behavior shown in Fig. 7. Fig. 9 shows that increasing the tortuosity values by a factor of 3/2 while leaving the other parameter values the same, improves the agreement of the SS and NUPSD predictions with data.

5. Conclusion

The objective of this research was to explore the acoustic characteristics of materials manufactured from wood chips. Direct measurements of the normal incidence absorption coefficient spectra of the samples were obtained using an impedance tube in the frequency range from 63 to 6300 Hz. Measurements were made on four different sample thicknesses (20, 30, 40, and 50 mm) composed from wood chips that passed through five different mesh sizes (4, 8, 10, 12, and 16). In addition, the porosity and flow resistivity of every sample were obtained using non-acoustical methods. Four analytical models for rigid-porous media were used for predictions corresponding to slanted parallel identical uniform slits (SS), Johnson-Champoux-Allard (JCA), Johnson-Champoux-Allard-Lafarge (JCAL) for arbitrary pore structures, and a non-uniform pore log-normal size distribution (NUPSD). To obtain the parameters, other than porosity and flow resistivity, required by JCA and JCAL, a differential evolution algorithm in MATLAB software and Finite Element Method (FEM) simulations in COMSOL software was used to fit the measured absorption coefficient spectra.

The principal results can be summarized as follows:

- Increasing thickness increases in the absorption coefficient and the quarter wavelength absorption peaks shift toward lower frequencies.
- The introduction of an air gap behind the sample increases absorption at lower frequencies. Since this can yield absorption coefficient spectra equivalent to those obtained with greater thickness it can reduce manufacturing costs.
- The wood chip samples have relatively low flow resistivities resulting in resonant absorption spectra even with the highest sample thickness.
- Increasing bulk density results in increased absorption, particularly at lower frequencies.
- Samples of a given thickness with smaller particle sizes have higher sound absorption corresponding to higher flow resistivity.
- For a given thickness, the first quarter wavelength resonance peaks in absorption coefficient spectra for the samples with smaller sizes

Table 5
Parameter values used in the predictions in Fig. 8.

Sample	Model	d mm	∅	σ Pa. s m^{-2}	α_∞	b μm	θ°	β	Λ μm	Λ' μm	$k_0' \times 10^8$
1	SS	20	0.725	5880	2.2	168.0	47.60	–	–	–	–
	NUPSD					–	–	1.475	–	–	–
	JCA					–	–	–	240	380	–
	JCAL					–	–	–			3.297
2	SS	30	0.725	5590	2.4	179.8	49.79	–	–	–	–
	NUPSD					–	–	1.554	–	–	–
	JCA					–	–	–	200	500	–
	JCAL					–	–	–			4.499
3	SS	40	0.725	5310	1.8	159.7	41.80	–	–	–	–
	NUPSD					–	–	1.273	–	–	–
	JCA					–	–	–	230	410	–
	JCAL					–	–	–			11.620
4	SS	50	0.725	4980	1.3	142.3	28.70	–	–	–	–
	NUPSD					–	–	0.851	–	–	–
	JCA					–	–	–	390	550	–
	JCAL					–	–	–			0.803
5	SS	20	0.696	6010	3.0	198.2	54.80	–	–	–	–
	NUPSD					–	–	1.741	–	–	–
	JCA					–	–	–	190	300	–
	JCAL					–	–	–			8.178
6	SS	30	0.696	5710	2.61	189.4	51.8	–	–	–	–
	NUPSD					–	–	1.627	–	–	–
	JCA					–	–	–	202	260	–
	JCAL					–	–	–			5.67
7	SS	40	0.696	5460	2.36	138	49.40	–	–	–	–
	NUPSD					–	–	1.539	–	–	–
	JCA					–	–	–	138	270	–
	JCAL					–	–	–			4.38
8	SS	50	0.696	5710	2.4	150.1	38.4	–	–	–	–
	NUPSD					–	–	1.554	–	–	–
	JCA					–	–	–	190	350	–
	JCAL					–	–	–			4.405
9	SS	20	0.684	6160	1.23	126.2	25.6	-	-	-	-
	NUPSD					-	-	0.756	-	-	-
	JCA					-	-	-	58	140	-
	JCAL					-	-	-			0.55
10	SS	30	0.684	5860	2.08	168.3	46.1	–	–	–	–
	NUPSD					–	–	1.421	–	–	–
	JCA					–	–	–	97	360	–
	JCAL					–	–	–			2.791
11	SS	40	0.684	5580	2.1	173.4	46.4	–	–	–	–
	NUPSD					–	–	1.431	–	–	–
	JCA					–	–	–	160	291	–
	JCAL					–	–	–			3.024
12	SS	50	0.633	6080	2.2	183	47.6	–	–	–	–
	NUPSD					–	–	1.475	–	–	–
	JCA					–	–	–	180	290	–
	JCAL					–	–	–			3.7
13	SS	20	0.661	6260	1.5	140.9	35.4	–	–	–	–
	NUPSD					–	–	1.058	–	–	–
	JCA					–	–	–	70	130	–
	JCAL					–	–	–			3.034
14	SS	30	0.661	5940	1.9	150.1	43.5	–	–	–	–
	NUPSD					–	–	1.331	–	–	–
	JCA					–	–	–	66	150	–
	JCAL					–	–	–			5.67
15	SS	40	0.661	5690	2.1	174.7	46.4	–	–	–	–
	NUPSD					–	–	1.431	–	–	–
	JCA					–	–	–	130	160	–
	JCAL					–	–	–			2.965
16	SS	50	0.661	5350	2.2	184.3	47.6	–	–	–	–
	NUPSD					–	–	1.475	–	–	–
	JCA					–	–	–	115	165	–
	JCAL					–	–	–			3.624
17	SS	20	0.633	6390	2.2	172.3	47.6	–	–	–	–
	NUPSD					–	–	1.475	–	–	–
	JCA					–	–	–	70	130	–
	JCAL					–	–	–			3.034
18	SS	30	0.633	6080	2.2	176.6	47.6	–	–	–	–
	NUPSD					–	–	1.475	–	–	–
	JCA					–	–	–	66	194	–
	JCAL					–	–	–			3.189
19	SS	40	0.633	5760	1.9	168.7	43.5	–	–	–	–

(continued on next page)

Table 5 (*continued*)

	NUPSD					–	–	1.331	–	–	–
	JCA					–	–	–	65	226	
	JCAL					–	–	–			2.169
20	**SS**	50	0.633	5410	1.96	176.8	44.42	–	–	–	–
	NUPSD					–	–	1.363	–	–	–
	JCA					–	–	–	75	350	–
	JCAL					–	–	–			2.536

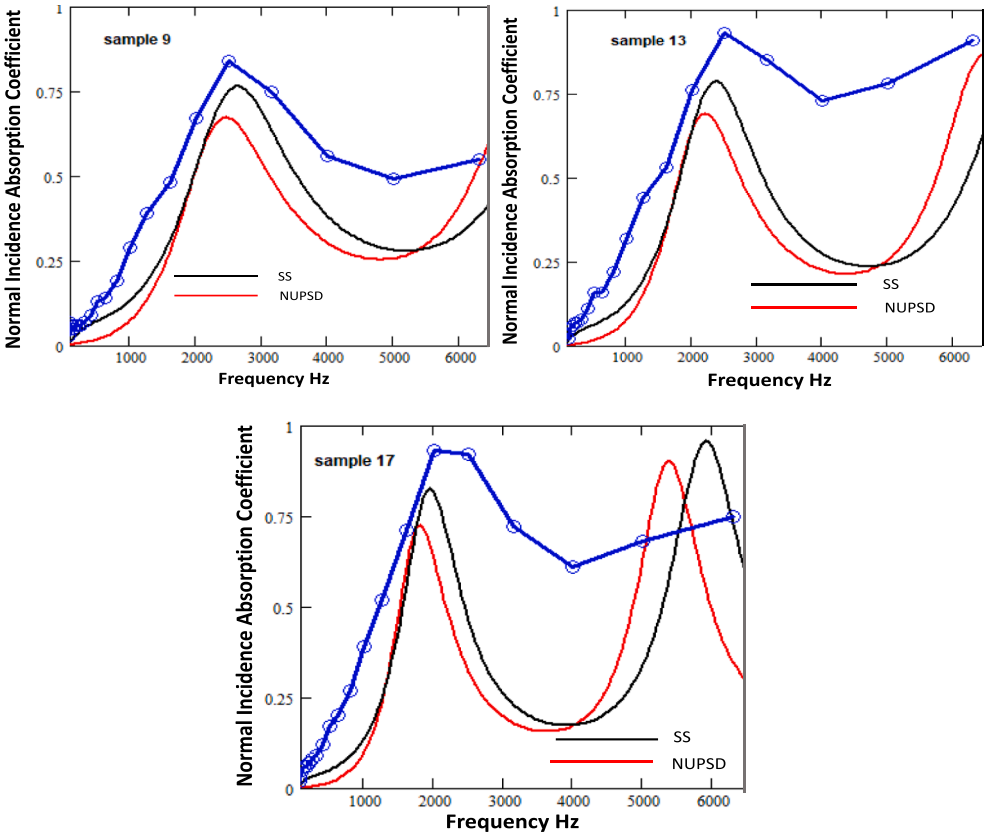

Fig. 9. Comparison of SS and NUPSD predictions with data for samples 9, 13, and 17 with JCA-fitted tortuosity increased by a factor of 3/2.

are at lower frequencies which is consistent with higher tortuosity even though the values obtained by fitting the JCA model to data are not consistent with this.

- Although the JCA and JCAL models offer the best agreement with data, the SS and NUPSD models give useful predictions despite requiring only one fitted parameter (tortuosity) in addition to the measured porosity and flow resistivity.
- For samples for which the SS and NUPSD predictions have a poorer agreement with data, increasing the fitted tortuosity values improves the agreement significantly.
- Sound absorbers made from wood chips could be useful for indoor applications.

CRediT authorship contribution statement

Maedeh Lashgari: Writing – original draft, Methodology, Investigation, Data curation, Conceptualization. **Ebrahim Taban:** Resources, Project administration, Investigation, Funding acquisition, Conceptualization. **Mohammad Javad SheikhMozafari:** Writing – original draft, Supervision, Project administration, Methodology, Investigation, Funding acquisition, Conceptualization. **Parham Soltani:** Supervision, Project administration. **Keith Attenborough:** Writing – review & editing, Software, Methodology, Investigation. **Ali Khavanin:** Supervision, Project administration, Methodology, Investigation, Conceptualization.

Declaration of competing interest

The authors declare that they have no known competing financial interests or personal relationships that could have appeared to influence the work reported in this paper.

Data availability

Data will be made available on request.

References

[1] Mj S, Mohammad Alizadeh P, Ahmadi O, Mazloomi B. Assessment of noise effect on employee comfort in an open-plan office: validation of an assessment questionnaire. J Occup Health Epidemiol 2021;10:193–203.
[2] Ileperuma D, Arachchige IR. Hearing status and noise exposure levels of Workers at a Laundry Plant in Sri Lanka. Audiol Speech Res 2022;18:95–101.
[3] Mj S, Ahmadi O. Reliability and validity assessment of the Persian version of the noise exposure questionnaire (NEQ): an NIHL predictor tool. J Occup Health Epidemiol 2022;11:209–22.
[4] Chen Z, Liu T. Development and application status of glass wool, rock wool, and ceramic wool. In: Thermal Insulation and Radiation Control Technologies for Buildings. Springer; 2022. p. 129–61.
[5] Yan Q, Meng Z, Luo J, Wu Z. Experimental study on improving the properties of rock wool and glass wool by silica aerogel. Energ Buildings 2021;247:111146.

[6] Karimi F, Soltani P, Zarrebini M, Hassanpour A. Acoustic and thermal performance of polypropylene nonwoven fabrics for insulation in buildings. J Build Eng 2022; 50:104125.
[7] Soltani P, Mirzaei R, Samaei E, NourMohammadi M, Gharib S, Abdi D, et al. Sound absorption characteristics of aluminosilicate fibers. Int J Environ Sci Technol 2022; 19:10245–56.
[8] Arenas JP, del Rey R, Alba J, Oltra R. Sound-absorption properties of materials made of esparto grass fibers. Sustainability 2020;12:5533.
[9] Arenas JP, Sakagami K. Sustainable acoustic materials. MDPI 2020:6540.
[10] Arenas JP. Applications of acoustic textiles in automotive/transportation. Acoust Text 2016,:143–63.
[11] Hajimohammadi M, Soltani P, Semnani D, Taban E, Fashandi H. Nonwoven fabric coated with core-shell and hollow nanofiber membranes for efficient sound absorption in buildings. Build Environ 2022;213:108887.
[12] Karimah A, Ridho MR, Munawar SS, Adi DS, Damayanti R, Subiyanto B, et al. A review on natural fibers for development of eco-friendly bio-composite: characteristics, and utilizations. J Mater Res Technol 2021;13:2442–58.
[13] Cucharero J, Ceccherini S, Maloney T, Lokki T, Hänninen T. Sound absorption properties of wood-based pulp fibre foams. Cellul 2021;28:4267–79.
[14] Smardzewski J, Kamisiński T, Dziurka D, Mirski R, Majewski A, Flach A, et al. Sound absorption of wood-based materials. Holzforschung 2015;69:431–9.
[15] Zhao X, Liu Y, Zhao L, Yazdkhasti A, Mao Y, Siciliano AP, et al. A scalable high-porosity wood for sound absorption and thermal insulation. Nat Sustainability 2023;6:306–15.
[16] Halashi K, Taban E, Soltani P, Amininasab S, Samaei E, Moghadam DN, et al. Acoustic and thermal performance of luffa fiber panels for sustainable building applications. Build Environ 2024;247:111051.
[17] SheikhMozafari MJ, Taban E, Soltani P, Faridan M, Khavanin A. Sound absorption and thermal insulation performance of sustainable fruit stone panels. Appl Acoust 2024;217:109836.
[18] Kassim DH, Putra A, Ramlan R. Enhancement of sound absorption of coir fiber using thin layer of kapok fibers. J Nat Fibers 2023;20:2164103.
[19] Fattahi M, Taban E, Soltani P, Berardi U, Khavanin A, Zaroushani V. Waste corn husk fibers for sound absorption and thermal insulation applications: a step towards sustainable buildings. J Build Eng 2023;77:107468.
[20] Jang E-S. Sound absorbing properties of selected green material—A review. Forests 2023;14:1366.
[21] Mehrzad S, Taban E, Soltani P, Samaei SE, Khavanin A. Sugarcane bagasse waste fibers as novel thermal insulation and sound-absorbing materials for application in sustainable buildings. Build Environ 2022;211:108753.
[22] Bousshine S, Ouakarrouch M, Bybi A, Laaroussi N, Garoum M, Tilioua A. Acoustical and thermal characterization of sustainable materials derived from vegetable, agricultural, and animal fibers. Appl Acoust 2022;187:108520.
[23] Kamal T, Wajih I, Sharma V, Rafat Y, Siddiqui M. Evaluation of agricultural waste natural fiber as an acoustic absorber for reduction of industrial noise. In: Ergonomics for Improved Productivity: Proceedings of HWWE 2017: Springer; 2021. p. 335–41.
[24] Samaei SE, Berardi U, Taban E, Soltani P, Mousavi SM. Natural fibro-granular composite as a novel sustainable sound-absorbing material. Appl Acoust 2021;181: 108157.
[25] Sengupta S, Basu G, Datta M, Debnath S, Nath D. Noise control material using jute (Corchorus olitorius): effect of bulk density and thickness. J Text Inst 2021;112: 56–63.
[26] Taban E, Mirzaei R, Faridan M, Samaei E, Salimi F, Tajpoor A, et al. Morphological, acoustical, mechanical and thermal properties of sustainable green Yucca (Y. gloriosa) fibers: an exploratory investigation. J Enviorn Health Sci Eng 2020;18: 883–96.
[27] da Silva CCB, Terashima FJH, Barbieri N, de Lima KF. Sound absorption coefficient assessment of sisal, coconut husk and sugar cane fibers for low frequencies based on three different methods. Appl Acoust 2019;156:92–100.
[28] Taban E, Tajpoor A, Faridan M, Samaei SE, Beheshti MH. Acoustic absorption characterization and prediction of natural coir fibers. Acoust Australia 2019;47: 67–77.
[29] Zhang J, Shen Y, Jiang B, Li Y. Sound absorption characterization of natural materials and sandwich structure composites. Aerospace 2018;5:75.
[30] Lim Z, Putra A, Nor MJM, Yaakob M. Sound absorption performance of natural kenaf fibres. Appl Acoust 2018;130:107–14.
[31] Samaei SE, Berardi U, Mahabadi HA, Soltani P, Taban E. Optimization and modeling of the sound absorption behavior of polyurethane composite foams reinforced with kenaf fiber. Appl Acoust 2023;202:109176.
[32] Bin Bakri MK, Jayamani E, Soon KH, Hamdan S, Kakar A. An experimental and simulation studies on sound absorption coefficients of banana fibers and their reinforced composites. Nano Hybrids Compos 2017;12:9–20.
[33] Berardi U, Iannace G. Predicting the sound absorption of natural materials: best-fit inverse laws for the acoustic impedance and the propagation constant. Appl Acoust 2017;115:131–8.
[34] Stinson MR. The propagation of plane sound waves in narrow and wide circular tubes, and generalization to uniform tubes of arbitrary cross-sectional shape. J Acoust Soc Am 1991;89:550–8.
[35] Biot MA. Theory of propagation of elastic waves in a fluid-saturated porous solid. II. Higher frequency range. J Acoust Soc Am 1956;28:179–91.
[36] Carman PC. Flow of gases through porous media. (No Title). 1956.
[37] Johnson DL, Koplik J, Dashen R. Theory of dynamic permeability and tortuosity in fluid-saturated porous media. J Fluid Mech 1987;176:379–402.
[38] Champoux Y, Stinson MR. On acoustical models for sound propagation in rigid frame porous materials and the influence of shape factors. J Acoust Soc Am 1992; 92:1120–31.
[39] Allard J. Propagation of sound in porous media. Amsterdam: Elsevier Science; 1993.
[40] Taban E, Soltani P, Berardi U, Putra A, Mousavi SM, Faridan M, et al. Measurement, modeling, and optimization of sound absorption performance of Kenaf fibers for building applications. Build Environ 2020;180:107087.
[41] Champoux Y, Allard JF. Dynamic tortuosity and bulk modulus in air-saturated porous media. J Appl Phys 1991;70:1975–9.
[42] Saati F, Hoppe K-A, Marburg S, Horoshenkov KV. The accuracy of some models to predict the acoustical properties of granular media. Appl Acoust 2022;185:108358.
[43] Horoshenkov KV, Groby J-P, Dazel O. Asymptotic limits of some models for sound propagation in porous media and the assignment of the pore characteristic lengths. J Acoust Soc Am 2016;139:2463–74.
[44] Hashemi Z, Esmailpour MM, Nasirzadeh N, Farvaresh E, Beigzadeh Z, Salari S. Estimation of sound absorption behavior of combined panels comprising Kenaf fibers and micro-perforated plates below 2500 Hertz. J Health Safety Work 2023; 12:872–94.
[45] Boubel A, Garoum M, Bousshine S, Bybi A. Investigation of loose wood chips and sawdust as alternative sustainable sound absorber materials. Appl Acoust 2021; 172:107639.
[46] Cherradi Y, Rosca IC, Cerbu C, Kebir H, Guendouz A, Benyoucef M. Acoustic properties for composite materials based on alfa and wood fibers. Appl Acoust 2021;174:107759.
[47] Berardi U, Iannace G. Acoustic characterization of natural fibers for sound absorption applications. Build Environ 2015;94:840–52.
[48] Prabhune S, Munde Y, Shinde A, Siva I. Appraising the acoustic performance and related factors of natural fiber: a review. J Nat Fibers 2022;19:13475–94.
[49] Attenborough K. Macro- and micro-structure designs for porous sound absorbers. Appl Acoust 2019;145:349–57.